tektonika

Supporting Information (SI) for "3D Interaction of Tectonics and Surface Processes Explains Fault Network Evolution of the Dead Sea Fault"

Esther L. Heckenbach[1,2]*, Sascha Brune[1,2]* & Anne C. Glerum[1]& Roi Granot[3]& Yariv Hamiel[4]& Stephan V. Sobolev[1,2]& Derek Neuharth[1,5]

[1]*Helmholtz Zentrum Potsdam - Deutsches GeoForschungsZentrum GFZ, Potsdam, Germany*
[2]*University of Potsdam - Institute of Geosciences, Potsdam, Germany*
[3]*Ben-Gurion University of the Negev, Beer-Sheva, Israel*
[4]*Geological Survey of Israel, Jerusalem, Israel*
[5]*ETH Zürich, Zürich, Switzerland*
**Corresponding authors (e-mail: hecken@gfz-potsdam.de, brune@gfz-potsdam.de)*

Contents

1 Numerical model

The geodynamic modeling was carried out using the open-source code ASPECT (Kronbichler et al., 2012; Heister et al., 2017; Gassmöller et al., 2018). In this study, it solves the incompressible flow equations of momentum, mass and energy (assuming an infinite Prandtl number) for velocity $\boldsymbol{v}$, pressure P and temperature T, combined with advection equations for each Eulerian compositional field c_i:

$$-\nabla \cdot (2\eta\dot{\epsilon}) + \nabla P = \rho \boldsymbol{g} \tag{1}$$

$$\nabla \cdot \boldsymbol{v} = 0 \tag{2}$$

$$\bar{\rho} c_P \left(\frac{\partial T}{\partial t} + \boldsymbol{v} \cdot \nabla T \right) - \nabla \cdot k \nabla T = \bar{\rho} H \qquad \text{radioactive heating} \tag{3}$$

$$+ (2\eta\dot{\epsilon}) : \dot{\epsilon} \qquad \text{shear heating}$$

$$+ \alpha T (\boldsymbol{v} \cdot \nabla P) \qquad \text{adiabatic heating}$$

$$\frac{\partial c_i}{\partial t} + \boldsymbol{v} \cdot \nabla c_i = 0, \tag{4}$$

where η is the effective viscosity (see Eq. 5-8), $\dot{\epsilon}$ is the deviator of the strain rate tensor $\frac{1}{2}(\nabla \boldsymbol{v} + (\nabla \boldsymbol{v})^T)$, density $\rho = \rho_0(1-\alpha(T-T_0))$ with T_0 the reference temperature, and $\boldsymbol{g}$ gravity. $\bar{\rho}$ is the adiabatic reference density, c_P the specific isobaric heat capacity, k the thermal conductivity, and α the thermal expansivity, as given in Table S1.

We use a visco-plastic rheology (Glerum et al., 2018) with dislocation and diffusion creep rheologies as well as the Drucker-Prager yield criterion. In 2D, these are implemented within ASPECT through the following equations:

$$\eta_{eff}^{comp} = \left(\frac{1}{\eta^{df}} + \frac{1}{\eta^{ds}} \right)^{-1} \qquad \text{composite viscosity} \tag{5}$$

$$\text{with} \quad \eta_{ds|df} = \frac{1}{2} A^{-\frac{1}{n_{ds|df}}} d^{\frac{m_{ds|df}}{n_{ds|df}}} \dot{\epsilon}_{ii}^{\frac{1-n_{ds|df}}{n_{ds|df}}} exp\left(\frac{E_{ds|df} + PV_{ds|df}}{n_{ds|df} RT} \right) \qquad \text{ds | df creep} \tag{6}$$

When $2\eta_{eff}^{comp}\dot{\epsilon} > \sigma_y$, the plastic effective viscosity (Eq. 7) is used instead of the composite effective viscosity (Eq. 5):

$$\eta_{eff}^{pl} = \frac{\sigma_y}{2\dot{\epsilon}_{ii}} \qquad \text{plastic effective viscosity} \tag{7}$$

$$\text{with} \quad \sigma_y = P \cdot sin(\phi) + C \cdot cos(\phi) \qquad \text{Drucker-Prager plasticity} \tag{8}$$

where η_{eff} is the effective viscosity, $ds|df$ corresponds to dislocation or diffusion creep, d is grain size, R is the gas constant, $A_{ds|df}$ are prefactors, $n_{ds|df}$ and $m_{ds|df}$ are stress and grain size exponents. For diffusion creep, $n_{df} = 1$, while for dislocation creep, $m_{ds} = 0$. $E_{ds|df}$ are the activation energies, $V_{ds|df}$ are the activation volumes, σ_y is the yield stress, ϕ is the internal angle of friction and C is cohesion. $\dot{\epsilon}_{ii}$ is defined as the square root of the second invariant of the deviatoric strain rate tensor. The final effective viscosity (Eq. 5 or Eq. 7) is capped by a user-defined minimum and maximum viscosity η_{min} and η_{max}. The parameters used are listed in Table S1.

Surface processes are simulated using FastScape (Braun and Willett, 2013; Yuan et al., 2019), which solves for the stream power law, hillslope diffusion and sedimentation:

$$\frac{\partial h}{\partial t} = U - K_f A^m S^n + \frac{G}{A} \int_A \left(U - \frac{\partial h}{\partial t} \right) dA + K_d \nabla^2 h \tag{9}$$

where h is topographic height, U uplift, S slope, and A the drainage area. These parameters evolve with the model run and are taken from the surface mesh. Prescribed parameters are K_f - the bedrock river incision rate, m - the drainage area exponent, n - the slope exponent, G - the bedrock deposition coefficient and K_d - the bedrock diffusivity. All values used are listed in Table S2. For details about the coupling of ASPECT and FastScape, we refer the reader to Neuharth et al. (2022a,b).

Table S1: *Material properties used in the geodynamic models. We assume a grain size of 1 mm that is included in the pre-exponential factors. These factors have further been converted from the experimental values to account for the usage of second invariants for strain rate and stress. The user-defined minimum and maximum viscosities are $\eta_{min} = 1 \cdot 10^{19}$ Pas and $\eta_{max} = 1 \cdot 10^{24}$ Pas.* [(a)] *Rutter and Brodie (2004),* [(b)] *Rybacki et al. (2006),* [(c)] *Hirth and Kohlstedt (2004). Frictional strain softening is used, where the friction angle reduces linearly from 30° to 7.5° for brittle strain between 0 and 1. For strains larger than 1, it remains constant at 7.5°.*

	Sediments (wet quartzite)	Upper crust (wet quartzite)	Lower crust (wet anorthite)	Lithospheric mantle (dry olivine)	asthenosphere (wet olivine)	Unit
Thermal properties						
thermal diffusivity κ	0.728	0.926	0.585	0.838	0.833	$mm^2\ s^{-1}$
heat capacitiy c_p		1200	1200	1200	1200	$J\ kg^{-1}\ K^{-1}$
density at surface conditions ρ	2118	2668	2835	3260	3300	$kg\ m^{-3}$
density at in-situ conditions ρ_0	2150	2750	2900	3300	3300	$kg\ m^{-3}$
thermal expansivity α	3.70	2.70	2.70	3.00	3.00	$10^{-5}\ K^{-1}$
radioactive heating H	1.2	1.5	0.2	0	0	$\mu W\ m^{-3}$
Dislocation creep	(a)	(a)	(b)	(c)	(c)	
prefactor A_{ds}	$8.57{\cdot}10^{-28}$	$8.57{\cdot}10^{-28}$	$7.13{\cdot}10^{-18}$	$6.54{\cdot}10^{-16}$	$2.12{\cdot}10^{-15}$	$Pa^{-n}\ s^{-1}$
stress exponent n_{ds}	4	4	3	3.5	3.5	-
activation energy E_{ds}	223	223	345	530	480	$kJ\ mol^{-1}$
activation volume V_{ds}	0	0	$3.80{\cdot}10^{-5}$	$1.80{\cdot}10^{-5}$	$1.10{\cdot}10^{-5}$	$cm^3\ mol^{-1}$
Diffusion creep	(a)	(a)	(b)	(c)	(c)	
prefactor A_{df}	$5.97{\cdot}10^{-19}$	$5.97{\cdot}10^{-19}$	$2.99{\cdot}10^{-25}$	$2.25{\cdot}10^{-9}$	$1.5{\cdot}10^{-9}$	$Pa^{-1}\ s^{-1}$
grain size exponent m_{df}	2	2	3	0	0	-
activation energy E_{df}	223	223	159	375	335	$kJ\ mol^{-1}$
activation volume V_{df}	0	0	$3.80{\cdot}10^{-5}$	$6.00{\cdot}10^{-6}$	$4.00{\cdot}10^{-6}$	$m^3\ mol^{-1}$
Drucker-Prager plasticity						
friction angle ϕ	30	30	30	30	30	°
cohesion C	20	20	20	20	20	MPa

Table S2: *Prescribed FastScape parameters for simulations including surface processes.*

	Value	Unit
Bedrock river incision rate K_f	$0.25{\cdot}10^{-5}$ / $0.5{\cdot}10^{-5}$ / $1{\cdot}10^{-5}$	$m^{0.2}/yr$
Bedrock diffusivity K_d	$1{\cdot}10^{-2}$	m^2/yr
Bedrock deposition coefficient G	1	-
Drainage area exponent m	0.4	-
Slope exponent n	1	-
Marine diffusivity	500	m^2/yr

2 Influence of inheritance

We represent small-scale inherited heterogeneity (rock type, weaknesses) with initial non-zero plastic strain. The initial plastic strain magnitude is obtained by multiplying random numbers on the 0–1 interval with a Gaussian distribution of a user-set amplitude and standard deviation perpendicular to the initial fault seeds. The random numbers are controlled by the seed of the random number generator. Varying this seed allows us to generate different initial conditions while keeping all other parameters constant. This holds interesting ramifications because our models show that some aspects of the final basin geometry are controlled by the localization of the first faults around the releasing bend. These modulate the final basin width and the interbasinal structures, but they also affect the asymmetry of the basement surface observed at the Dead Sea, which has been subject to much discussion (Quennell, 1959; Garfunkel, 1981; Ben-Avraham and Zoback, 1992; Wdowinski and Zilberman, 1996; Lubberts and Ben-Avraham, 2002; DESERT Group et al., 2004). Figure S1 shows that minor variations in crustal heterogeneities can play a significant role in shaping the basin (compare Fig. S1a,c,e, with b,d,f). However, the asymmetric basement topography is a constant in all presented model results. We therefore suggest that the general asymmetry of the Dead Sea Basin is an inevitable consequence of this particular geological setting, while the details of its actual shape may be influenced by smaller-scale and less-predictable processes.

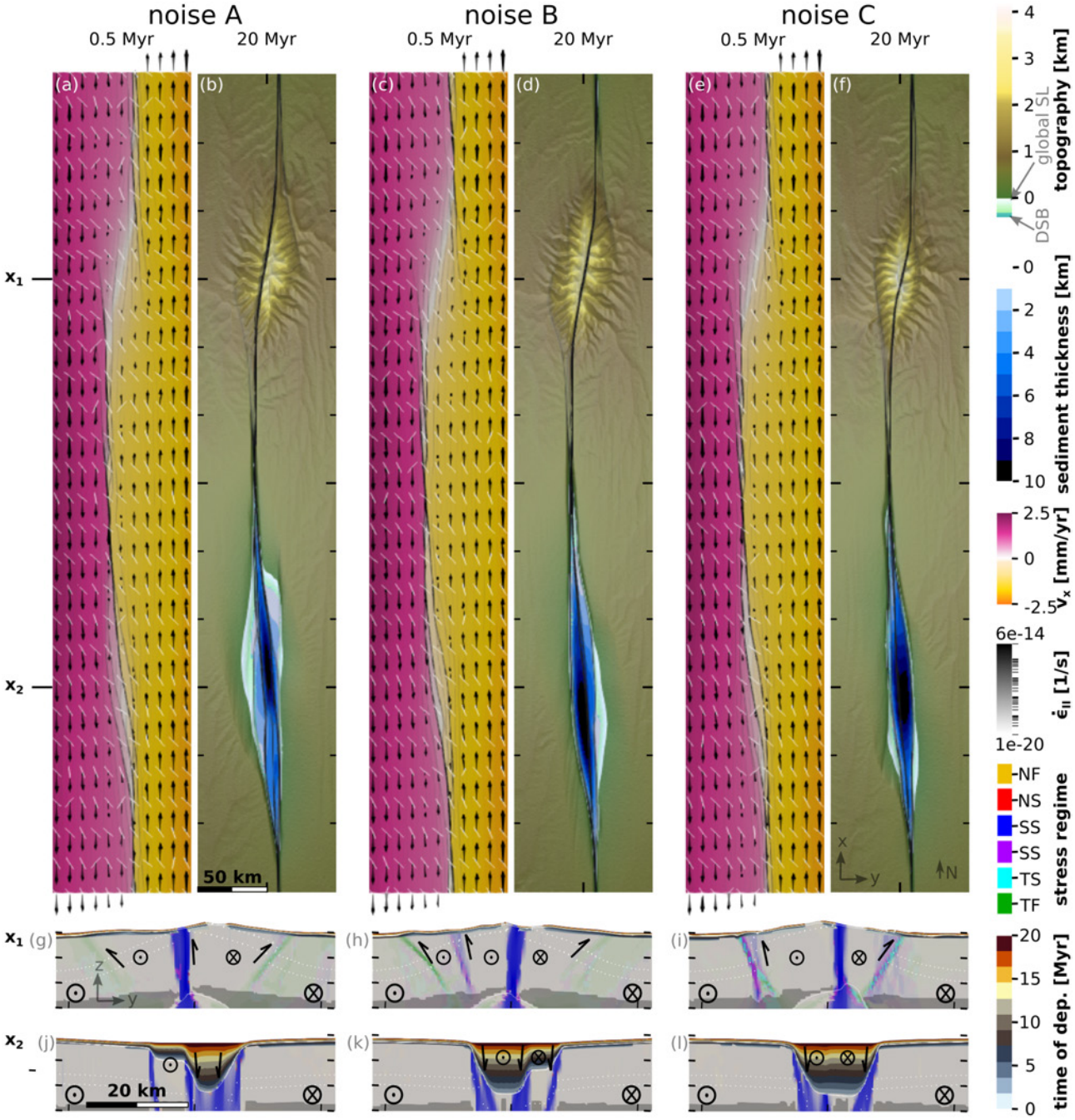

Figure S1: *Models using different values for the seed of the random noise in initial strain, described with noise A,B,C. (a), (c), (e) Fault-parallel velocity v_x=v_{II} in colour overlain by strain rate in black during the localization phase at 0.5 Myr. The black arrows depict magnitude and direction of the surface velocity, while the white bars show the direction of maximum horizontal compressive stress. (b), (d), (f) Surface topography and sediment thickness overlain by strain rate in black at the end of the model runs at 20 Myr. (g–l) Upper crustal profiles of the stress regime at the locations of the initial stepovers at x_1 = 150 km and x_2 = 450 km at 20 Myr. Brighter colours correlate with higher strain rates. Lighter areas deform in a brittle, darker areas in a ductile manner. Sediment age is shown in a separate colour scale. Black arrows demonstrate relative motions of fault-separated blocks.*

3 Influence of the boundary velocity

The reference model has a full strike-slip velocity of 5 mm/yr. We furthermore explored a variation of ± 10%, resulting in velocities of 4.5 and 5.5 mm/yr. These values are within the range of observed and assumed velocity variations for both present day and geological strike-slip motion of the Dead Sea area (Le Beon et al., 2008; Hamiel and Piatibratova, 2019, 2021). For a more generic exploration of the influence of the boundary velocity, we also ran models with 2.5 mm/yr and 10 mm/yr, which is equivalent to half and double the reference velocity (Fig. S2). All models were run to the same amount of total displacement of 100 km.

Faster boundary velocities increase basin volume through timing of fault localization. Running the model with double or half the reference boundary velocity to the same amount of total displacement shows that velocity has a larger impact on the resulting basin than the coupling to surface processes. While varying the surface process efficiency mainly affects the topography of the surface and basement, the boundary velocity also has a major impact on the fault network that manifests during the localization phase. At the releasing bend of the slow model with a total strike-slipe velocity of 2.5 mm/yr, the fault localizes as a straight surface trace without many bends, no branching and no deep basin (Fig. S2a,f). Contrarily, in the fast model with 10 mm/yr (Fig. S2e,j), many faults quickly localize simultaneously and form a mosaic of blocks. The basin quickly elongates and deepens, forming a basin that is wider and deeper than the reference model basin (Fig. S2r vs. t). This relationship between opening velocity and sediment volume has also been described for other types of basins (Berry et al., 2019). For the more DSB-like variations of the boundary velocity of 5 mm/yr ± 10% (Fig. S2b,d), we see similar trends. Overall, the sediment thickness shows an almost linear relationship with the boundary velocity, where a variation of 0.5 mm/yr changes the sediment thickness by ∼1 km. This increase in sediment volume can likely be explained by the fast localization of several faults in the models with greater strike-slip motion. As described in Section 3.1 of the main manuscript, rapid subsidence and sediment accumulation only start with the formation of a second border fault around a distinct crustal block at the location of the future pull-apart basin. While many of these blocks exist early in the fastest model (by ∼4 km of strike-slip displacement), the one in the slowest model forms later (∼10 km of strike-slip displacement), which limits sediment accumulation and subsidence.

Faster boundary velocities increase mountain heights and decrease off-fault deformation. At the fault network of the restraining bend, it is noticeable that lower boundary velocities result in longer bordering faults that take up more displacement. This goes hand in hand with the central connecting fault becoming decreasingly important with decreasing velocity. While this central fault is long-lived in most models, in the fastest model (10 mm/yr) several mountain cutting faults exist that are short-lived as the fault network evolves (Fig. S2j,o). Except for the fastest model, a decrease in the boundary velocity makes the fault-generated crustal block separation more diffuse and the fault trace more edgy (Fig. S2f–i,k–n). While a smoothening fault trace should reduce compressive stresses and therefore uplift, mountain heights in our models increase with increasing velocity. This trend can be explained by the balancing of tectonic and erosional forces and their temporal components (e.g. Willett, 1999). The faster the boundary velocity, the shorter the time for erosion to reduce elevations. For slower strike-slip velocities on the other hand there is more time for erosion to outbalance tectonic uplift. More erosion should hence provide a higher amount of sediments available to fill the pull-apart basin. However, this is not what we observe in our model series (Fig. S2p–t). Instead, the models show that sediment thickness is tightly bound to the timing of the formation of a fault-bounded basin floor, and therefore to the interaction of stress, strain and strain rate during the localization phase which limits the depositional space.

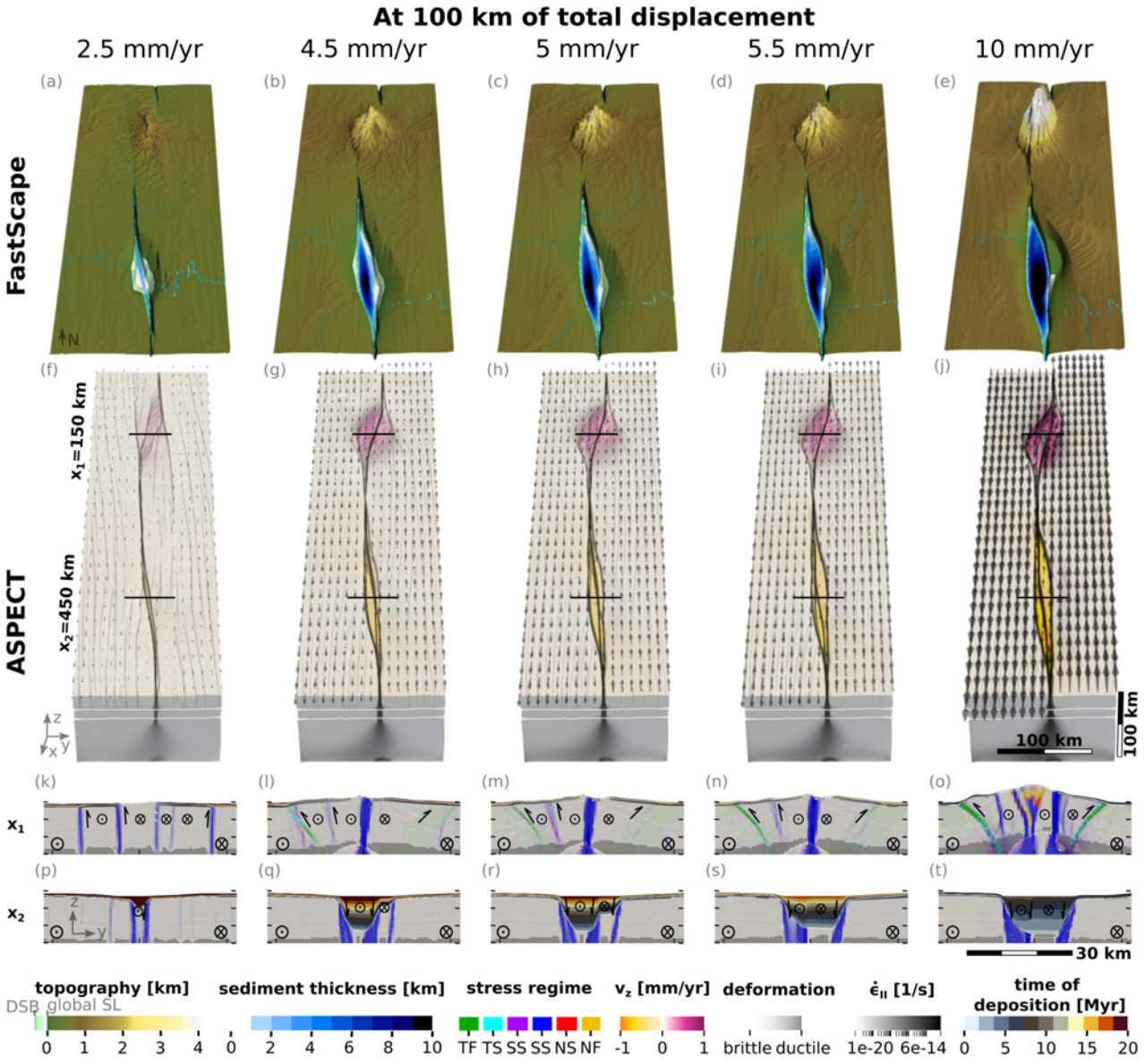

Figure S2: *Final state of models that were run to a total strike-slip displacement of 100 km using different boundary velocities (i.e., different velocities need a different amount of time to reach 100 km of displacement). Full strike-slip velocities and model times range from (a) 2.5 mm/yr over 40 Myr to (e) 10 mm/yr over 10 Myr. The reference model in this paper uses (c) 5 mm/yr over 20 Myr. (a–e) topography, drainage network and sediment thickness. (f–j) vertical velocities shown in colour scale and overlain by strain rate in black and and arrows depicting the magnitude and direction of velocities in the x-y-plane. White lines show layer thicknesses. (k–o) profiles through the restraining bend and (p–t) profiles through the releasing bend. Their location is shown in (f–j). Stress regime is shown as a colour scale with brighter colours indicating higher strain rates. Light areas deform in a brittle and dark areas in a ductile manner. Arrows depict relative motion similar to geological cross sections. Sediment age is indicated in a separate colour scale within the basin. The white dotted lines show the current location of the initially horizontal layer of particles used as deformation markers.*

4 Influence of temporal changes in the boundary velocity

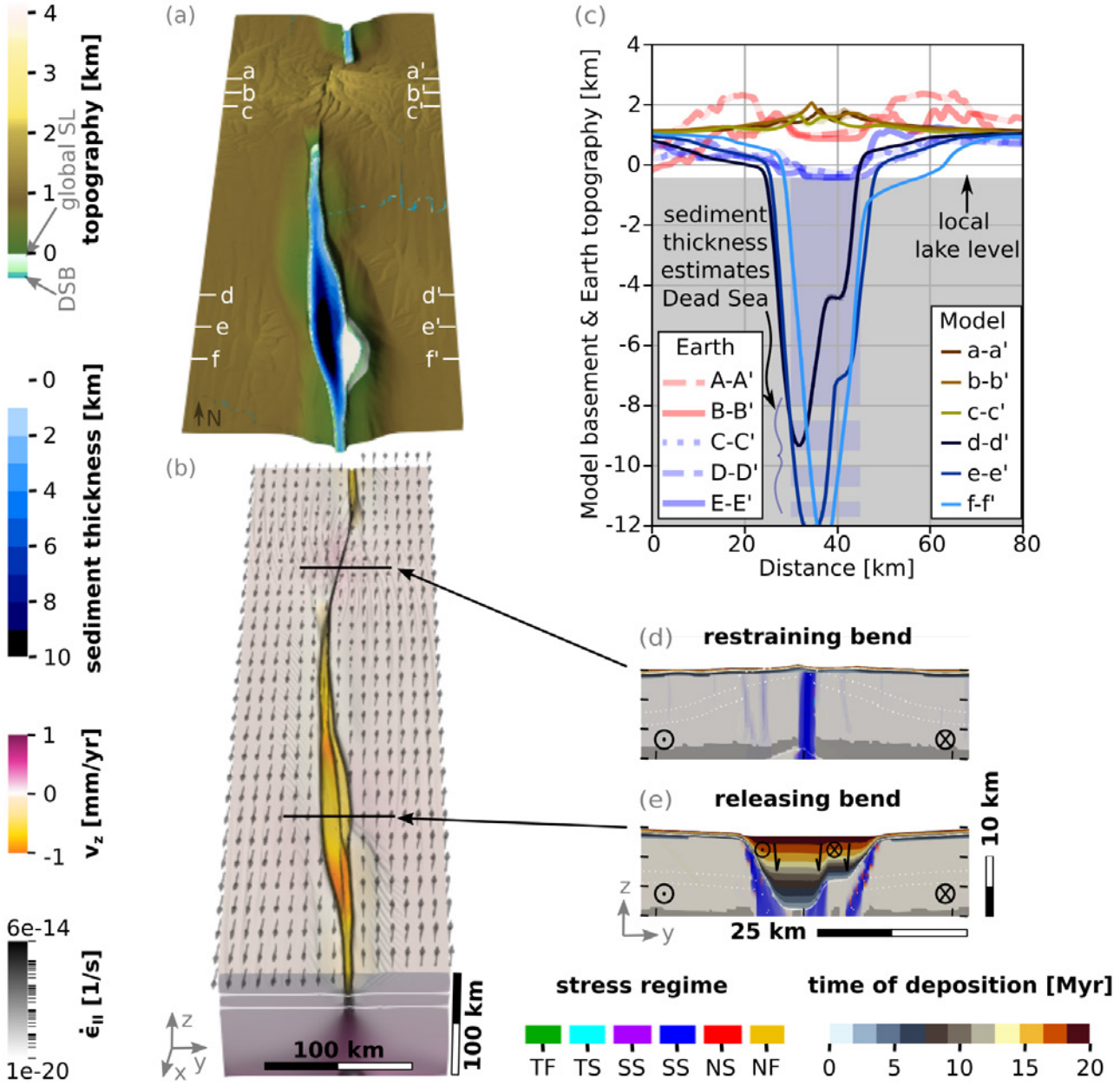

Figure S3: *Plots of a model that equals the reference model until 15 Myr and has afterwards been restarted until 20 Myr with extension included in the boundary velocity. Extension equals 10% of the strike-slip velocity, so 0.5 mm/yr.* ***(a)*** *topography and sediment thickness.* ***(b)*** *vertical velocity and strain rate pattern. Almost no surface uplift occurs.* ***(c)*** *cross sections comparing model topography (locations shown in a) with the topography of the Dead Sea Basin locations shown in Fig. 4d of the main article) It can be seen that the model basin becomes wider and the mountains smaller than at the DSB.* ***(d–e)*** *cross sections at the restraining and the releasing bend showing the stress regime and the sediment age. The colors of the stress regime are more intense for areas with high strain rate.*

5 Vertical axis rotations

Observed shortening at the Lebanese restraining bend amounts to only 5 km. This is relatively small, which is attributed to a 22–60° counterclockwise rotation of blocks around a vertical axis (Dembo et al., 2021a). The same applies to our model's restraining bend, showing only minor shortening in the fault-parallel direction but substantial rotation around the z-axis close to the faults. We attribute this rotation to the offset in initial weaknesses representing inherited structures (Glerum et al., 2020). As suggested for the Lebanese mountains (Gomez et al., 2007), the main part of our modeled rotation happens before the mountain-cutting fault forms, while strain partitioning emerges after this event. Model rotation of the block to the west of the central fault in the restraining bend amounts to 15–30°, while we see only 5–15° next to the basin border faults. With paleomagnetic data from the Hula and Kinneret releasing stepovers (see Fig. 4a in main article for location) indicating rotation magnitudes of 4–32° (Dembo et al., 2021b), the model block rotations are at the lower end of observations for both types of bends. Both predicted and observed rotation is clockwise in between the faults and anticlockwise otherwise.

6 Seismicity patterns

Concerning deep seismicity, our models show high strain-rate values along the basin bordering faults that induce local rheological changes towards a brittle regime at usually ductily behaving depths (Supplementary Fig. S4). In our models, this analog to deep earthquakes exists in combination with relatively high surface heat flow values. Indeed, we find that ∼45% of the brittle energy dissipation rate resides in the layer below 20 km depth, which is consistent with 40% of observed micro-earthquakes nucleating below 20 km (Aldersons et al., 2003).

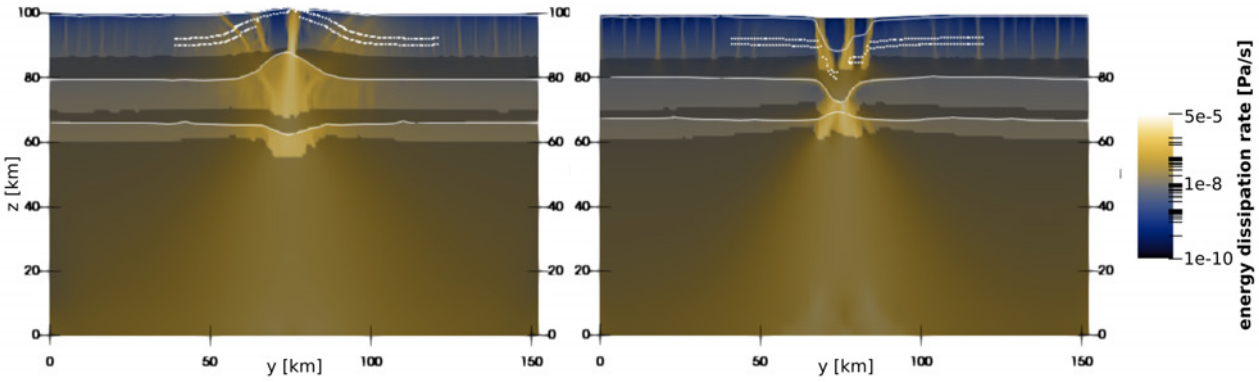

Figure S4: *Cross sections at the restraining bend (x = 150 km) and the releasing bend (x = 450 km) showing the energy dissipation rate, which has been used as a model analog of the energy released by all earthquakes during the length of one time step (Petrunin et al., 2012). Layer outlines are shown as white lines and tracked particle locations as white dots to visualize deformation. Lighter areas behave in a brittle and darker areas behave in a ductile way.*

7 Crustal deformation patterns

Crustal thinning and thickening occur near the releasing bend and restraining bend, respectively (Fig. 6 of the main manuscript). Thinning and thickening are correlated with the efficiency of surface processes. To assess its impact, we compared the three models using different surface process efficiencies and the model without any surface processes (Fig. 5 of the main text) as well as a model without erosion but with

marine sedimentation regarding their crustal thickness changes over 20 Myr. Here we provide more details for our analysis (Table S3). Below the pull-apart basin at the main fault, thinning in the model without surface processes amounts to 23%. However, when sedimentation is taken into account, the amount of crustal thinning increases to 38%. When erosion and sedimentation are included, thinning ranges between 40–41% for K_f between $0.25{\cdot}10^{-5}$ to $1{\cdot}10^{-5}$ $m^{0.2}$/yr. It should be noted that the lower crust experiences stronger thinning of $\sim$75%, while it is $\sim$15% for the upper crust. Below the highest elevations at the restraining bend, crustal thickening amounts to 39% for the purely geodynamic model, but is reduced to 24% for the reference model and to 16% for the model with high surface process efficiency. Crustal thickening at the restraining bend therefore shows a much stronger correlation with K_f than crustal thinning at the releasing bend. Moreover, while the lower crust is thickening more intensively for higher surface process efficiency with values between 85% and 106%, the upper crust experiences thinning for all models with erosion, and it only thickens when erosion is not accounted for. The thinning is more intensive for higher surface process efficiency (15% for K_f=0.25 $m^{0.2}$/yr, 45% for K_f=$1{\cdot}10^{-5}$ $m^{0.2}$/yr), which is a combined effect of erosion and increased uplift as described above. It is also the reason why at this place the amount of total crustal thickening decreases for higher surface process efficiencies. Additionally to these prominent changes directly at the restraining and the releasing bend, we also observe thinning and thickening of the crust away from the fault network. 25 km to the east of the pull-apart basin, crustal thinning increases with surface process efficiency just as below the basin, but it has values ranging between 6–16%. However, thinning of the upper crust amounts to $>$30% for all models including sedimentation. Contrarily, the lower crust experiences increasing thickening with increasing surface process efficiency ranging between 8–23%. Thickening of the lower crust surrounding the releasing bend is probably induced by the high amount of lower crustal thinning below the basin. 50 km to the east of the restraining bend, crustal thickening in both the lower and the upper crust amounts to $\sim$4% and slightly decreases with surface process efficiency. One exception from the low values is the upper crust of the purely geodynamic model without surface processes, which is thickened by 33%.

Table S3: *Influence of the surface process efficiency on changes in crustal thickness for four locations. Values are given in percentage (%) of the initial layer thickness. Negative values indicate crustal thinning, positive values stand for crustal thickening. A value of 0 means no change in thickness, while -100% means complete thinning, while +100% means that the layer's thickness has doubled. The change in crustal thickness has been computed with* $\Delta t = -(t_0 - t_{20})/t_0$*, where* t_0 *is the initial thickness and* t_{20} *the thickness at 20 Myr. It can be seen that thinning and thickening mostly increases with increasing surface process efficiency. An opposite trend only exists at the restraining bend, for whole crustal thickness changes at y = 74 and 125 km and upper crustal changes at y = 125 km.*

		Restraining bend x = 150 km		**Releasing bend** x = 450 km	
	surface process efficiency	**at the fault** y = 74 km	**surrounding** y = 125 km	**at the fault** y = 74 km	**surrounding** y = 100 km
upper crust	none	7	33	7	-2
	only sedimentation	6	5	-13	-3
	low	-14	4	-16	-3
	medium (ref model)	-26	5	-16	-3
	high	-45	2	-16	-4
lower crust	none	85	3	-68	1
	only sedimentation	85	3	-75	1
	low	105	5	-75	2
	medium (ref model)	98	4	-76	2
	high	106	4	-77	2
whole crust	none	39	4	-23	-1
	only sedimentation	38	4	-38	-2
	low	30	4	-40	-1
	medium (ref model)	24	4	-41	-1
	high	16	2	-41	-1

8 Animation

An animation of the reference model can be found at https://zenodo.org/doi/10.5281/zenodo.10405076. On the left side, the evolution of topography and sediment thickness are shown in two complementing color scales as a 3D surface. In the middle, cross sections of the stress regime at the two stepovers at x_1 = 150 km and x_2 = 450 km are shown. The white dotted lines show the initially horizontal layers of particles that are used as deformation markers. The line graphs on top show the x-, y- and z-components of the surface velocities of the two cross sections. On the right side, map views of topography, stress regime and boundary parallel velocity v_x are provided, from left to right, respectively. All three are overlain by strain rate. For more information on the parameters, see Fig. 5 of the main text.

References

Aldersons, F., Ben-Avraham, Z., Hofstetter, A., Kissling, E., and Al-Yazjeen, T. (2003). Lower-crustal strength under the Dead Sea basin from local earthquake data and rheological modeling. *Earth and Planetary Science Letters*, 214(1):129–142.

Ben-Avraham, Z. and Zoback, M. D. (1992). Transform-normal extension and asymmetric basins: An alternative to pull-apart models. *Geology*, 20(5):423–426.

Berry, M., van Wijk, J., Cadol, D., Emry, E., and Garcia-Castellanos, D. (2019). Endorheic-Exorheic Transitions of the Rio Grande and East African Rifts. *Geochemistry, Geophysics, Geosystems*, 20(7):3705–3729.

Braun, J. and Willett, S. D. (2013). A very efficient O(n), implicit and parallel method to solve the stream power equation governing fluvial incision and landscape evolution. *Geomorphology*, 180-181:170–179.

Dembo, N., Granot, R., and Hamiel, Y. (2021a). Mechanical contrast and asymmetric distribution of crustal deformation across plate boundaries: Insights from the northern Dead Sea fault system. *Geology*, 49(5):498–503.

Dembo, N., Hamiel, Y., and Granot, R. (2021b). The stepovers of the Central Dead Sea Fault: What can we learn from the confining vertical axis rotations? *Tectonophysics*, 816:229036.

DESERT Group, Weber, M., Abu-Ayyash, K., Abueladas, A., Agnon, A., Al-Amoush, H., Babeyko, A., Bartov, Y., Baumann, M., Ben-Avraham, Z., Bock, G., Bribach, J., El-Kelani, R., Förster, A., Förster, H.-J., Frieslander, U., Garfunkel, Z., Grunewald, S., Götze, H. J., Haak, V., Haberland, C., Hassouneh, M., Helwig, S., Hofstetter, A., Jäckel, K.-H., Kesten, D., Kind, R., Maercklin, N., Mechie, J., Mohsen, A., Neubauer, F. M., Oberhänsli, R., Qabbani, I., Ritter, O., Rümpker, G., Rybakov, M., Ryberg, T., Scherbaum, F., Schmidt, J., Schulze, A., Sobolev, S., Stiller, M., Thoss, H., Weckmann, U., and Wylegalla, K. (2004). The crustal structure of the Dead Sea Transform. *Geophysical Journal International*, 156(3):655–681.

Garfunkel, Z. (1981). Internal structure of the Dead Sea leaky transform (rift) in relation to plate kinematics. *Tectonophysics*, 80(1):81–108.

Gassmöller, R., Lokavarapu, H., Heien, E., Puckett, E. G., and Bangerth, W. (2018). Flexible and Scalable Particle-in-Cell Methods With Adaptive Mesh Refinement for Geodynamic Computations. *Geochemistry, Geophysics, Geosystems*, 19(9):3596–3604.

Glerum, A., Brune, S., Stamps, D. S., and Strecker, M. R. (2020). Victoria continental microplate dynamics controlled by the lithospheric strength distribution of the East African Rift. *Nature Communications*, 11(1):2881.

Glerum, A., Thieulot, C., Fraters, M., Blom, C., and Spakman, W. (2018). Nonlinear viscoplasticity in ASPECT: benchmarking and applications to subduction. *Solid Earth*, 9(2):267–294.

Gomez, F., Nemer, T., Tabet, C., Khawlie, M., Meghraoui, M., and Barazangi, M. (2007). Strain partitioning of active transpression within the Lebanese restraining bend of the Dead Sea Fault (Lebanon and SW Syria). *Geological Society, London, Special Publications*, 290(1):285–303.

Hamiel, Y. and Piatibratova, O. (2019). Style and Distribution of Slip at the Margin of a Pull-Apart Structure: Geodetic Investigation of the Southern Dead Sea Basin. *Journal of Geophysical Research: Solid Earth*, 124(11):12023–12033.

Hamiel, Y. and Piatibratova, O. (2021). Spatial Variations of Slip and Creep Rates Along the Southern and Central Dead Sea Fault and the Carmel–Gilboa Fault System. *Journal of Geophysical Research: Solid Earth*, 126(9):e2020JB021585.

Heister, T., Dannberg, J., Gassmöller, R., and Bangerth, W. (2017). High Accuracy Mantle Convection Simulation through Modern Numerical Methods. II: Realistic Models and Problems. *Geophysical Journal International*, 210(2):833–851.

Hirth, G. and Kohlstedt, D. (2004). Rheology of the Upper Mantle and the Mantle Wedge: A View from the Experimentalists. In *Inside the Subduction Factory*, pages 83–105. American Geophysical Union (AGU).

Kronbichler, M., Heister, T., and Bangerth, W. (2012). High Accuracy Mantle Convection Simulation through Modern Numerical Methods. *Geophysical Journal International*, 191:12–29.

Le Beon, M., Klinger, Y., Amrat, A. Q., Agnon, A., Dorbath, L., Baer, G., Ruegg, J.-C., Charade, O., and Mayyas, O. (2008). Slip rate and locking depth from GPS profiles across the southern Dead Sea Transform. *Journal of Geophysical Research: Solid Earth*, 113(B11).

Lubberts, R. K. and Ben-Avraham, Z. (2002). Tectonic evolution of the Qumran Basin from high-resolution 3.5-kHz seismic profiles and its implication for the evolution of the northern Dead Sea Basin. *Tectonophysics*, 346(1):91–113.

Neuharth, D., Brune, S., Glerum, A., Morley, C. K., Yuan, X., and Braun, J. (2022a). Flexural strike-slip basins. *Geology*, 50(3):361–365.

Neuharth, D., Brune, S., Wrona, T., Glerum, A., Braun, J., and Yuan, X. (2022b). Evolution of Rift Systems and Their Fault Networks in Response to Surface Processes. *Tectonics*, 41(3):e2021TC007166.

Petrunin, A. G., Meneses Rioseco, E., Sobolev, S. V., and Weber, M. (2012). Thermomechanical model reconciles contradictory geophysical observations at the Dead Sea Basin. *Geochemistry, Geophysics, Geosystems*, 13(4).

Quennell, A. M. (1959). Tectonics of the dead sea rift. In *Proceedings of the 20th international geological congress, Mexico*, pages 385–403.

Rutter, E. H. and Brodie, K. H. (2004). Experimental grain size-sensitive flow of hot-pressed Brazilian quartz aggregates. *Journal of Structural Geology*, 26(11):2011–2023.

Rybacki, E., Gottschalk, M., Wirth, R., and Dresen, G. (2006). Influence of water fugacity and activation volume on the flow properties of fine-grained anorthite aggregates. *Journal of Geophysical Research: Solid Earth*, 111(B3).

Wdowinski, S. and Zilberman, E. (1996). Kinematic modelling of large-scale structural asymmetry across the Dead Sea Rift. *Tectonophysics*, 266(1):187–201.

Willett, S. D. (1999). Orogeny and orography: The effects of erosion on the structure of mountain belts. *Journal of Geophysical Research: Solid Earth*, 104(B12):28957–28981.

Yuan, X. P., Braun, J., Guerit, L., Simon, B., Bovy, B., Rouby, D., Robin, C., and Jiao, R. (2019). Linking continental erosion to marine sediment transport and deposition: A new implicit and O(N) method for inverse analysis. *Earth and Planetary Science Letters*, 524:115728.